Wall-modeled large-eddy simulations of the HIFiRE-2 scramjet

I. Bermejo-Moreno, J. Larsson, J. Bodart, Ronan Vicquelin

Wall-modeled large-eddy simulations of the HIFiRE-2 scramjet

By I. Bermejo-Moreno, J. Larsson, J. Bodart AND R. Vicquelin

1. Motivation and objectives

Research and development of hypersonic air-breathing vehicles capable of sustained operation in flight have received renewed interest by the international scientific community in the past decade. The series of HyShot flight experiments performed by the Centre for Hypersonics at the University of Queensland, Australia, in the early 2000s demonstrated successful flight operation of a scramjet engine for a time period of 6 to 10 seconds at Mach 7.5 and led to the HyCAUSE joint project between the United States Defense Advanced Research Projects Agency (DARPA) and the Australian Defence, Science and Technology Organisation (DSTO), also focused on scramjet operation (at Mach 10). These two pioneering programs culminated in the on-going Hypersonic International Flight Research Experimentation Program (HIFiRE), a collaborative effort among the United States Air Force Research Laboratory (AFRL), NASA, and the Australian DSTO. NASA's X-43 aircraft and the on-going Boeing X-51 WaveRider (a collaborative effort with the AFRL, DARPA, NASA, and Pratt & Whitney) are also among the suite of recent experimental programs on hypersonic scramjet-based propulsion.

The HIFiRE program (see Jackson *et al.* 2011, for an overview) comprises a set of eight flight tests, the second of which (HIFiRE-2) was intended to demonstrate transition from dual-mode to scram-mode operation over a flight Mach range from 6 to 8 at nearly constant dynamic pressure, achieving a combustion efficiency of at least 70% in the scram-mode. The flight test, successfully flown in May 2012, was supported by a campaign of ground tests (Hass *et al.* 2009; Cabell *et al.* 2011) performed in the HIFiRE Direct Connect Rig (HDCR) at the NASA Langley Arc-Heated Scramjet Test Facility (AHSFT). Additionally, computational fluid dynamics (CFD) simulations of the HDCR using Reynolds-Averaged Navier Stokes (RANS) solvers were performed to complement the ground tests in the design and development of the flowpath for the flight experiment (Storch *et al.* 2011; Bynum & Baurle 2011). Besides the aforementioned mode transition (i.e., operation at variable Mach number from dual to scramjet operation), other key elements that set the HIFiRE scramjet apart from its predecessors are the use of a hydrocarbon fuel (versus the hydrogen fuel used in HyShot and HyCAUSE programs), a multi-staged fuel injection system, and the presence of a cavity-based flame-holder located in between the two injection stages.

While low-fidelity, RANS simulations are a powerful engineering tool valuable in the design phases of these experimentation programs, higher-fidelity simulation techniques are required to discern the physical phenomena dominating at the different turbulence scales present in the flow (Fulton *et al.* 2012). Turbulent mixing, which plays a central role in supersonic combustion, and the unsteadiness due to large-scale turbulent motions, which can lead to flow instabilities inside the engine, are two such phenomena for which higher-fidelity simulations provide superior predicting capabilities than RANS. With today's computational power, direct numerical simulation (DNS) techniques that

resolve all the physical scales cannot yet be applied to solve the flow inside a scramjet. Large-eddy simulations (LES), aimed at resolving the larger spatial scales while modeling the smallest, unresolved scales, have recently been used in several numerical studies of scramjets (Berglund & Fureby 2007; Koo 2011; Fureby 2012; Larsson *et al.* 2011, 2012). Besides the subgrid scale models needed in any LES to account for the unresolved turbulent scales, the presence of turbulent boundary layers developed along the walls of any internal, high-Reynolds-number flow also requires modeling the near-wall turbulent structures in order to lower the otherwise unfeasible mesh resolution requirements of most practical flows of interest (see Choi & Moin 2012). Wall models (Kawai & Larsson 2012, 2013) or hybrid simulation techniques, such as Detached Eddy Simulations (DES) (Spalart 2009), are among the possible modeling alternatives. Furthermore, combustion models are necessary to account for the chemical reactions that take place inside the scramjet, due to the small characteristic time and length scales at which they occur in comparison with the achievable scales in an LES. The complexity of the chemical mechanism of a hydrocarbon fuel such as the one used in HIFiRE-2, involving a large number of species and chemical reactions, also adds to the need for a tractable combustion modeling approach.

In this brief, we present our current progress in the large-eddy simulation of the HIFiRE-2 scramjet at two operating conditions using an equilibrium wall model and flamelet-based combustion models. Larsson *et al.* (2012) successfully applied a similar methodology to simulate the flow inside the HyShot II scramjet. The HIFiRE-2 experiment adds new levels of physical complexity with respect to HyShot II and appears as a further independent validation case to challenge the models and numerical methods developed for high-fidelity simulations of supersonic reacting flows. In Section 2 we introduce the scramjet geometry and the experimental flow conditions targeted in the simulations. The description of the computational setup and the simulation methodology follows in Section 3. Results are presented in Section 4, including comparisons with available experimental data and exploration of instantaneous flow features. We end with the conclusions of this on-going work and present an outlook of future directions in Section 5.

2. Experimental geometry and flow conditions

Figure 1 shows a side view of the geometry of the HIFiRE-2 scramjet engine, including the isolator and combustor stages. The overall length is 711.3 mm, with a constant width of 101.6 mm. The isolator comprises nearly one third of the total length of the engine and has a constant height of 25.4 mm, whereas the top and bottom walls (body and cowl sides, respectively) of the combustor diverge at a constant, total angle of 2.6°. Two opposed cavity flameholders are located in the combustor, separating the two fuel injection stages, each with eight injection ports (four on the body side and four on the cowl side, equispaced spanwise). The primary injectors, located upstream of the cavity, are angled at a 15° inclination from the wall, with a circular diameter of 3.175 mm. Secondary injectors, located downstream of the cavity, are perpendicular to the wall with a 2.38 mm circular diameter. Cavity injectors were also included in the experimental design, although they were not active for the operating conditions under consideration in this brief, and will not be included in the simulations.

Since data from the HIFiRE-2 flight test have not yet been released, in this work we target the ground test experiments performed at the HDCR facility. Two experimental conditions are considered, as summarized in Table 1. These conditions correspond to

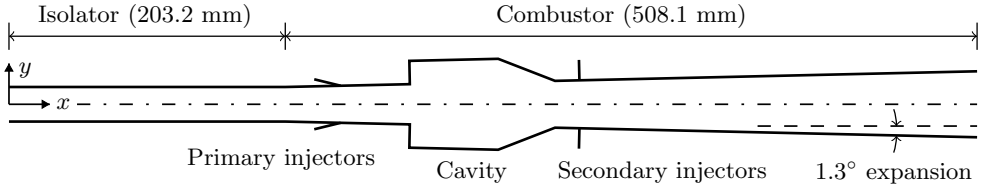

FIGURE 1. Schematic representation of the HIFiRE scramjet, including the isolator and combustor. Flow from left to right.

Test ID	M_f	M_n	$\dot{m}_{\text{air}}$	$\dot{m}_{f1}$	$\dot{m}_{f2}$
125.1	6.5	2.51	1.137	0.0291	0.0437
136.1	8.0	3.46	0.912	0.0234	0.0354

TABLE 1. Flow configurations for the two ground tests targeted in the simulations. M_f, simulated flight Mach number; M_n, HDCR nozzle Mach number; $\dot{m}_{\text{air}}$, air mass flow rate; $\dot{m}_{f1}$ and $\dot{m}_{f2}$, fuel mass flow rate in the primary and secondary injection stages, respectively. Mass flow rates in kg/s.

the experimental runs labeled 125.1 and 136.3 (see Hass *et al.* 2009; Cabell *et al.* 2011) for the simulated flight Mach numbers of 6.5 and 8.0, respectively, representative of the two operational modes of the HIFiRE-2 system (i.e., dual-mode and scram-mode). To simulate the Mach conditions achieved in flight for those operational modes, two different nozzles with varying exit Mach numbers (2.51 and 3.46 for the two tests considered, respectively) are utilized, feeding the isolator entrance directly and connecting it with the upstream arc-heater and mixing chamber of the HDCR facility. Hass *et al.* (2009) note that the matching of in-flight conditions by the ground tests is achieved only in a one-dimensional sense. Thus, a number of other in-flight flow features are not matched, including reflected shocks from the forebody/inlet processing, boundary layer thickness, surface temperatures, temperature time-history, and ingested air composition. An important consideration regarding the latter is that, as a result of arc-heating the incoming air in the ground test facility, nitric oxide is present in the test gas, which is known to enhance combustion (see Pellett *et al.* 2009, and references therein).

3. Computational setup and methodology

The spatially filtered compressible Navier-Stokes equations for the conserved variables of mass, momentum, and total energy (which includes sensible, kinetic, and chemical energy for the reacting flow) are solved in the present simulations using a finite volume formulation on unstructured hexahedral meshes. The solver implements a solution-adaptive methodology that combines a non-dissipative centered numerical scheme and an essentially non-oscillatory (ENO) second-order shock-capturing scheme (with an HLLC Riemann solver for the computation of the Euler fluxes), which is applied only in regions near shock waves identified by a shock sensor activated according to the criterion: $-\partial u_k/\partial x_k > \max(\sqrt{\omega_j\omega_j}, 0.05c/\Delta)$, where $\partial u_k/\partial x_k$, $\omega_j\omega_j$ and c are the local dilatation, enstrophy, and sound speed, respectively, and Δ is the control volume size. Additionally,

the shock-capturing scheme is applied in cells where differences with adjacent cells in mixture fraction or temperature are greater than 0.4 and 2500 K, respectively. Away from discontinuities, the non-dissipative (second-order) scheme is applied. A mesh-based blend of centered and upwind numerical schemes is used for robustness (Khalighi *et al.* 2011). Subgrid scale stresses are modeled following Vreman (2004). Gradient-diffusion models are used for the subgrid scale heat flux and species transport with fixed turbulent Prandtl and Schmidt numbers of 0.9. Subgrid-scale model terms are set to zero where the shock-capturing scheme is active (i.e., in regions marked by the shock sensor), to avoid adding extra dissipation to the already dissipative ENO scheme. A three-stage, third-order explicit Runge-Kutta algorithm is used to advance the discretized equations in time.

The computational domain includes the isolator and combustor stages of the scramjet. Horizontal and vertical center planes of symmetry ($y = 0$ and $z = 0$, respectively) are used to reduce the computational cost, by simulating only one quarter of the scramjet, including one of the engine sidewalls (at $z = 50.8$ mm). Two ports (at $z = 12.7$ and 38.1 mm) are modeled at each one of the primary and secondary fuel injection stages (at $x = 243.7$ and 419.1 mm, respectively). The reference system is chosen such that the origin of the streamwise coordinate, x, coincides with the inflow plane of the isolator; y is the vertical coordinate, with origin on the horizontal symmetry plane; and z is the spanwise coordinate, with origin on the vertical symmetry plane.

Three meshes of increasing resolution are used in the production runs of these simulations, with 12, 55, and 250 million control volumes. For all meshes, the grid spacing is refined near the walls, fuel injectors (meshed using O-grids), and in the region of development of the shear layer in the cavity.

3.1. *Combustion model*

To model combustion, the flamelet-progress variable approach (FPVA) of Pierce & Moin (2004), with the extensions for supersonic combustion of Terrapon *et al.* (2009, 2010) and Pečnik *et al.* (2012), was initially utilized in our simulations. The FPVA model reduces the otherwise computationally intractable complexity of a hydrocarbon fuel chemical mechanism (owing to the large number of species and reactions involved) to a flamelet look-up table, pre-computed for a set of flame boundary conditions. Transport/reaction equations are added to the filtered Navier-Stokes equations in the numerical solver for three additional scalar fields: the filtered mixture fraction, $\tilde{Z}$; the subgrid-scale variance of the mixture fraction, $\widetilde{Z''Z''}$; and a filtered reaction progress variable, $\tilde{C}$. The effects of turbulence in the subgrid fluctuations of the mixture fraction and progress variable are modeled by assuming β and δ probability density functions, respectively, in the integration of combustion variables in $ZC-$space leading to their filtered counterparts. In the present work, the progress variable is defined as the sum of the mass fractions of the following combustion products: H_2O, CO_2, CO, and H_2, and normalized between 0 (non-reacting) and 1 (fully reacted), for the set of flamelets conforming the library.

The flamelet library utilized to construct the look-up table is pre-computed using the FlameMaster code (Pitsch 2006) to solve the steady-state form of the flamelet equations, by assuming a counterflow diffusion flame configuration. Boundary conditions of pressure and temperature must be specified to solve the flamelet equations: presently, a constant background pressure of 170 KPa is used, which is representative of the average levels found experimentally in the HIFiRE-2 combustor for the operating regimes under consideration; the temperatures on the fuel and oxidizer sides are fixed at 300 K and 1300 K, respectively. Unity Lewis numbers (implying equal diffusivities for all species

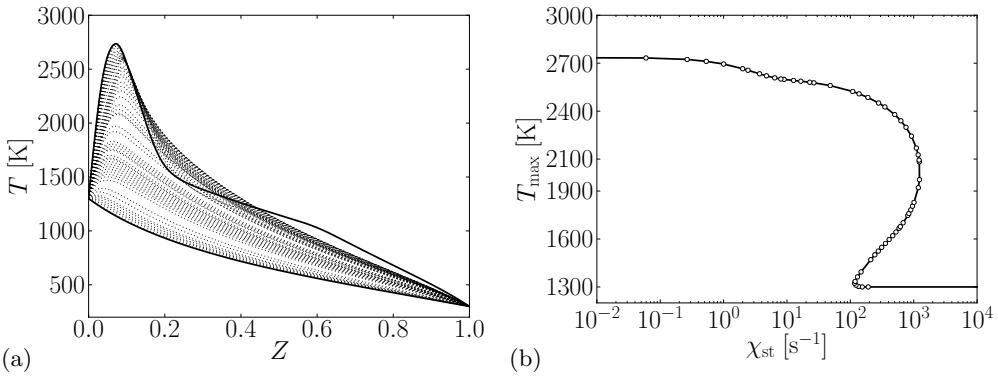

FIGURE 2. (a) Temperature profiles for the different flamelets obtained from the CEFRC v. 0.9 mechanism, varying between the fully quenched and fully reacted solutions (plotted in thicker lines). (b) S-shaped curve formed by the locus of maximum temperature as a function of stoichiometric scalar dissipation rate for each flamelet (in hollow circles).

and temperature) are considered. Following Pitsch *et al.* (1998), the effects of radiation are neglected in the flamelet library, since the steady-flamelet equations cannot account for the regime in which radiation becomes important (i.e., when the characteristic radiation time is shorter than the diffusion and residence times): the error incurred by the overprediction of the temperature resulting from neglecting radiation is smaller than the otherwise unrealistic effect of radiation at low scalar dissipation rates.

While this modeling approach has proven successful in simulations of subsonic combustion, its applicability to supersonic flows, where large variations of pressure and enthalpy can occur, is compromised. To partially account for the effects of compressibility, Terrapon *et al.* (2010) proposed the following modifications, which are also used in the present simulations: 1) the temperature in the flow solver is calculated from the filtered total energy. A linear expansion of the ratio of specific heats in terms of the temperature is used to eliminate the non-linear dependency between temperature and total energy, which introduces another approximation. From the calculated filtered temperature, the pressure is computed using an ideal gas equation of state. 2) Regarding the effect of pressure variations in the chemical state, the source term in the progress variable equation is scaled by the square of pressure. The applicability of such rescaling for a hydrocarbon fuel like the JP-7 surrogate utilized in the HIFiRE-2 scramjet is, however, questionable.

A volumetric mixture of 64% ethylene and 36% methane is used in the HIFiRE-2 scramjet as a two-component gaseous surrogate of partially-cracked JP-7, seeking to approximate its ignition delay, extinction, and flame strength characteristics. The CEFRC v. 0.9 mechanism provided by the High Temperature Gasdynamics Laboratory (HTGDL) at Stanford University (CEFRC 2013) was used to generate the flamelet library for the simulations presented in this brief. The mechanism consists of approximately 260 reactions and 50 species. Figure 2(a) shows the temperature profiles as a function of mixture fraction obtained for each flamelet included in the library computed with the CEFRC v. 0.9 mechanism. Figure 2(b) shows the maximum temperature for each flamelet as a function of the stoichiometric scalar dissipation rate, χ_{st}, that corresponds to each flamelet, recovering a characteristic S-shaped curve containing the upper, steady burning branch (stable), the intermediate (unstable) burning branch, and the lower (extinction) branch.

Radiation effects are not accounted for in the present simulations. Previous studies

found a negligible flow cooling due to radiative heat transfer in hydrogen-based scramjets with short flow residence times (Crow *et al.* 2012). However, the combination of longer residence times experienced in the cavity flameholder and the use of a hydrocarbon fuel in the HIFiRE-2 scramjet might result in radiation cooling playing a non-negligible role. From an a posteriori radiation analysis performed on a subset of solution files from our simulations, Crow (2013) found that temperature losses on the order of 10 to 100 K due to radiation can occur for fluid particles entrained in the recirculation zones of the flow. While their radiation analysis was done on an earlier subset of our simulations performed with a flamelet look-up table computed from the USC Mech version II chemical mechanism (111 species and 784 reactions) developed by Wang *et al.* (2007), the conclusions are not expected to vary significantly for the present simulations using the newly developed CEFRC mechanism.

Multi-feed injection systems, such as the one present in the HIFiRE-2 combustor with primary and secondary injection stages each containing multiple ports, might require additional mixture fractions to be transported, depending on the composition and conditions at the different injection stages (Doran 2011). Presently, only one mixture fraction is considered for all injection ports included in our simulations.

The FPVA combustion modeling strategy presented so far was successfully applied by Larsson *et al.* (2012) in the wall-modeled LES of the HyShot II scramjet, by using a different chemical mechanism corresponding to the hydrogen fuel used by HyShot. As will be shown in Section 4, our attempts to apply it to the HIFiRE-2 simulations failed for both operating regimes under consideration. Insufficient burning was found, particularly upstream of the cavity flameholder. Different pressure and temperature conditions used to construct the flamelet library were evaluated but led to equally unsuccessful results. In the ground test experiments, spark plugs were active to help initiate combustion, as it was found that ignition with primary fuel only could not be achieved (see Cabell *et al.* 2011). Several attempts were made in the simulations to replicate the effect of spark plugs (e.g., by adding an extra source term of progress variable localized near the spark plug), but burning was still insufficient.

A simplification of the FPVA model described above, which uses only the fully reacted flamelet from the library ($\widetilde{C} = 1$), was subsequently tested. Note that the flamelet solution at the boundary states of pure oxidizer and pure fuel concides with the fully quenched (non-reacting) flamelet ($\widetilde{C} = 0$). The temperature profiles as a function of the mixture fraction corresponding to these two limiting flamelets ($\widetilde{C} = 0$ and 1) are plotted in solid thick lines in Figure 2(a). This simplification is effectively equivalent (see Pierce 2001) to assuming that chemical kinetics are infinitely fast relative to the other flow phenomena (mixing, in particular). As a consequence, the equation for the filtered progress variable in the flow solver is no longer used. The other two additional scalar transport equations of the original combustion model, for the filtered mixture fraction and the subgrid-scale variance, are still kept. The latter includes the effects of turbulent mixing in the reaction processes. With this simplification of the combustion model, results for the dual-mode operating regime were better able to reflect the experimental data. Some comments on the possible implications of these findings will be presented in Section 5.

Alternatives to the FPVA approach have been applied in the literature in supersonic combustion. For example, Donde *et al.* (2012) and Koo *et al.* (2013) developed a Eulerian probability density function (PDF) for LES that uses a semi-discrete quadrature method of moments and applied it to simulate the flow inside a model scramjet including a

cavity flameholder and ethylene as fuel. They found qualitative agreement of the pressure profiles with experimental data.

3.2. *Wall model*

The wall model proposed by Kawai & Larsson (2012) is used in the present simulations. It solves the equilibrium boundary-layer equations in a refined, near-wall inner grid embedded in the coarser, background LES grid. The inner, wall-model simulation takes the filtered density, wall-parallel velocity, and temperature flow variables from the LES at a specified wall-normal distance as the outer boundary condition. After the boundary-layer equations are solved, the LES takes the wall shear stress and temperature or heat-flux (for an adiabatic or isothermal boundary condition, respectively) from the wall-model solution. In the present simulations, the walls are considered adiabatic (in the ground test experiments, a zirconia thermal barrier coating is applied on the walls (Cuda & Hass 2009)). The wall model is applied on all walls, excluding the injection ports.

The equilibrium assumption of the wall model implies that temporal, convective, pressure-gradient, and wall-parallel diffusion terms are neglected in its formulation of the boundary layer equations. This assumption greatly simplifies the equations to be solved, changing their character from partial to ordinary differential equations. However, non-equilibrium effects are present in the near-wall flow inside a scramjet (e.g., pressure gradients generated by shock waves, secondary flows near the corners, etc.). The successful application of this equilibrium wall model formulation in previous internal supersonic flows (Larsson *et al.* 2011, 2012; Bermejo-Moreno *et al.* 2011) suggests that such non-equilibrium effects can still be accounted for, at least partially, through the outer, LES-resolved part of the turbulent boundary layers. The cavity flameholder of the HIFiRE-2 configuration leads to massive flow separation and reattachment, for which the applicability of this simplified equilibrium wall model still needs to be proven. Alternative, more complete wall model formulations that do not assume equilibrium have been proposed in the literature (see, for example, Cabot 1995; Balaras *et al.* 1996; Wang & Moin 2002; Kawai & Larsson 2013), by retaining one or multiple additional terms neglected under the equilibrium assumption.

3.3. *Inflow*

The boundary condition at the inflow plane of the isolator matches the air mass flow rates and Mach numbers given in Table 1. Turbulent boundary layers develop upstream of the isolator along the forebody/inlet present in the flight tests and the HDCR nozzle present in the ground tests. Hass *et al.* (2009) noted that the incoming boundary layers of the ground tests are significantly thinner than those generated by the flight inlet. Presently we consider a nominal boundary layer thickness of approximately 1 mm at the entrance of the isolator. The turbulent nature of the boundary layers can significantly enhance the mixing of incoming air with the injected fuel in the primary stage and delay separation by better withstanding adverse pressure gradients. To account for these effects, in the present simulations we employ a synthetic turbulent inflow generator based on a digital filtering technique originally proposed by Klein *et al.* (2003), with the improvements of Xie & Castro (2008) and Touber & Sandham (2009). Two-dimensional mean velocity, pressure and temperature profiles are imposed at the cross-sectional inflow plane, along with turbulent fluctuations synthetically generated according to two-dimensional profiles of single-point correlation, and two-point correlations that reflect specified turbulent lengthscales (of the order of the incoming boundary layer thickness) in each coordinate direction. Since no experimental data regarding the incoming turbulent boundary layer

properties were available to feed the synthetic turbulence generator of the simulations, we used rescaled profiles from the supersonic flow inside a duct presented in Bermejo-Moreno *et al.* (2011).

3.4. *Fuel injection*

Characteristic boundary conditions for velocity, pressure, and temperature are used for the primary and secondary injectors, matching the experimental fuel mass flow rates specified in Table 1. In the experiments, the fuel was heated to prevent liquification of the ethylene present in the mixture (see Hass *et al.* 2009). In the simulations, the fuel temperature is set to 300 K. The injection system in the experiment was designed to operate with choked injectors. However, due to an a posteriori modification of the inlet, dual-mode operating conditions resulted in the primary injectors being unchoked experimentally. For this case ($M_f = 6.5$), the boundary condition for the primary injectors in the simulation was modified to relax the pressure, which adjusts to the value of the subsonic surrounding environment. The filtered mixture fraction and progress variable are set to 1 (pure fuel) and 0 (non-reacting), respectively. The variance of the subgrid-scale mixture fraction is set to zero.

4. Results

In this section we present first a comparison of time-averaged simulation results with available experimental data from the ground tests. Afterward, several flow features are explored by looking at instantaneous fields obtained from different snapshots of the simulations.

4.1. *Time-averaged pressure profiles. Comparison with experiments*

The HDCR is instrumented with static pressure ports along the isolator and combustor walls. Figure 3 shows a comparison of the time-averaged wall pressure profiles obtained from the simulations and the ground test experimental data at the spanwise center plane. In the simulations, statistics are collected for approximately 2 ms after initial transients, which corresponds to approximately 4.5 flow-through times for the flight Mach number of 6.5, based on the centerline velocity at the entrance to the isolator.

4.1.1. *Dual-mode*

For the dual-mode operation at $M_f = 6.5$, the simulations are started from quiescent flow in the non-reacting regime (without fuel injection). The hollow symbols and dash-dotted line in Figure 3(a) correspond to the experiments and (coarse-mesh) simulation results for that non-reacting (tare) case. The shape of the pressure profile is well captured by the simulation. The pressure recovery along the cavity ramp appears higher in the simulations, which might be a result of differences in the reattachment location with respect to the experiments associated with the wall model.

The reacting-flow simulation at $M_f = 6.5$ using the FPVA model (dash-dot-dotted line) is not capable of reproducing the pressure rise observed in the experiments (solid symbols), which starts upstream of the primary injection. In the simulation, the pressure rise occurs farther downstream, inside the cavity, and reaches levels much lower than in the experiments, indicating insufficient combustion. Downstream of the secondary injector, the pressure rises eventually and decays following a similar trend to the experimental profile, but at lower pressure levels.

Results with the flamelet-based fast-chemistry combustion model are shown for the

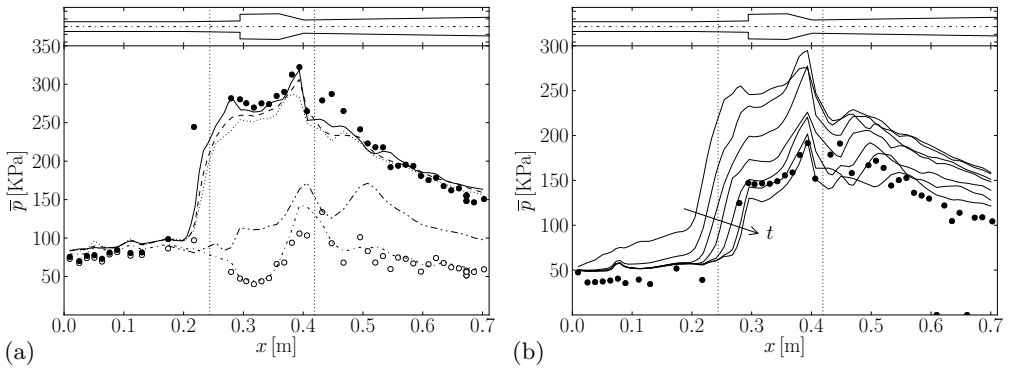

FIGURE 3. Time-averaged wall-pressure profiles at the center plane. (a) Dual-mode regime at $M_f = 6.5$: symbols correspond to the experiment (hollow for non-reacting and solid for reacting), and lines correspond to simulation results: dash-dotted for non-reacting; dash-dot-dot for reacting with original FPVA formulation; dotted, dashed and solid for reacting with flamelet-based fast-chemistry combustion model on coarse-, medium-, and fine-resolution meshes, respectively. (b) Transition from dual- to scram-mode: symbols, experimental data at $M_f = 8.0$; lines, WMLES results with flamelet-based fast-chemistry combustion model on medium-resolution mesh, with each line corresponding to the simulation data averaged over consecutive time intervals of 0.3 ms, evolving from the sudden change of conditions from dual- to scram-mode. For reference, a side view of the geometry of the scramjet is shown on top of each plot, along with vertical dotted lines indicating the primary and secondary stages of fuel injection.

three grid resolutions under consideration (in dotted, dashed, and solid lines, for increasing resolution). Better agreement with the experimental data is observed, recovering the pressure levels inside the cavity and in the last two thirds of the secondary combustor. The simulation results capture the pressure rise occurring upstream of the primary injector, although it is still found somewhat downstream of its corresponding experimental location, which penetrates farther into the isolator. A similar outcome was found by Bynum & Baurle (2011) who performed an uncertainty quantification study of the variability of the HIFiRE-2 ground test for the dual-mode regime (at a lower $M_f = 5.84$) through a series of 35 RANS simulations, showing that the combustion-induced shock system in the isolator appeared farther downstream in their simulations than in the ground tests. As mentioned in Section 2, the nitric oxide that results from the arc-heating of the test gas and is present in the incoming air flow entering the isolator in the ground tests Hass *et al.* (2009) might be responsible for enhancing combustion (Pellett *et al.* 2009), which could contribute to the combustion-induced pressure rise occurring farther upstream in the isolator. The simulations do not currently account for any possible incoming nitric oxide.

The pressure level in the combustor (particularly inside the cavity) increases slightly with mesh resolution, approaching the experimental results. This likely indicates that the results are not yet grid-converged. However, we note that the results for the fine-mesh simulation have been averaged for a shorter time period than the medium- and coarse-mesh simulations (2 ms), as the fine-mesh simulation is still running at the time of writing this brief.

4.1.2. *Scramjet-mode*

In the flight test, a continuous acceleration from the dual- to the scram-mode takes place during the several seconds of engine operation. In the ground tests, a different nozzle

needs to be used for each operating regime, so no transition between the two modes can be simulated in the HDCR facility. The computational expense associated with running the numerical simulations for longer than a few milliseconds makes it impractical, for the current mesh resolution and computational power considered in this brief, to simulate the mode transition for the extended duration of the flight test. Instead, from the solution of the dual-mode simulations at $M_f = 6.5$ presented in Section 4.1.1, a sudden change in the boundary conditions at the entrance to the isolator and the fuel injectors is imposed to match the scramjet operation at $M_f = 8$ in the ground tests. The flow then evolves through a transient reflected in Figure 3(b), which shows center-line wall-pressure profiles averaged over consecutive time intervals of 0.3 ms. It is observed that within the first 2 ms, the pressure levels throughout the scramjet decrease to the experimental values. In contrast to the dual-mode simulations, the scramjet simulations presented in this section have not yet reached a statistically stationary regime at the time of writing this brief: the pressure level reached in the cavity at the last time-interval shown in Figure 3(b) is already below the experimental data, suggesting that the combustion model in use (even with the fast-chemistry assumption) might not be able to sustain the supersonic combustion inside the scramjet in this operating mode. This issue is currently being investigated.

4.2. *Instantaneous flow features*

In this section we explore some of the flow features found in the numerical simulations. First, we focus on the dual-mode simulation that we later compare qualitatively with the scram-mode simulation at the instant of closest agreement with the experimental pressure profiles.

4.2.1. *Dual-mode at $M_f = 6.5$*

Figure 4 shows a three-dimensional view of the engine walls and vertical slices on one of the injection planes, with contours of several fields mapped at a particular instant of the $M_f = 6.5$ fine-mesh simulation. The turbulent nature of the boundary layers as they develop along the walls of the isolator is visible through the contours of wall-parallel velocity magnitude passed to the wall model. The magnitude of the density gradient on the vertical plane shows the oblique shock generated at the end of the isolator, whereas the temperature field in the upper symmetric vertical slice confirms that mixing and combustion occur in a recirculation region upstream of the primary injector. This can be seen better in Figure 5(a-b).

The concentration of species for different combustion products is shown in Figure 5(c, d and h) and also confirms the combustion-induced origin of the pressure increase upstream of the primary injection. Peak values of OH are seen near the wall in the cavity ramp, where the wall-pressure levels are higher (see Figure 3a) and the mixture fraction is closer to its stoichiometric value (enveloped by the black lines in Figure 5e). In contrast, H_2O shows a more homogeneous concentration inside the first part of the cavity (i.e., the part with the nearly constant cross section), decreasing along the cavity ramp; CO concentration (shown in Figure 5h for a plane parallel to the combustor wall separated 2 mm from it) peaks first along the initial part of the combustor, upstream of the cavity. The mixture fraction (Figure 5e) appears relatively more uniform inside the cavity (where the maximum temperatures are reached) than downstream of the secondary injection, where large-scale unsteadiness is present and results in more complex mixing and combustion patterns, which are also observed in the contours of the density-gradient magnitude and the concentration of combustion products.

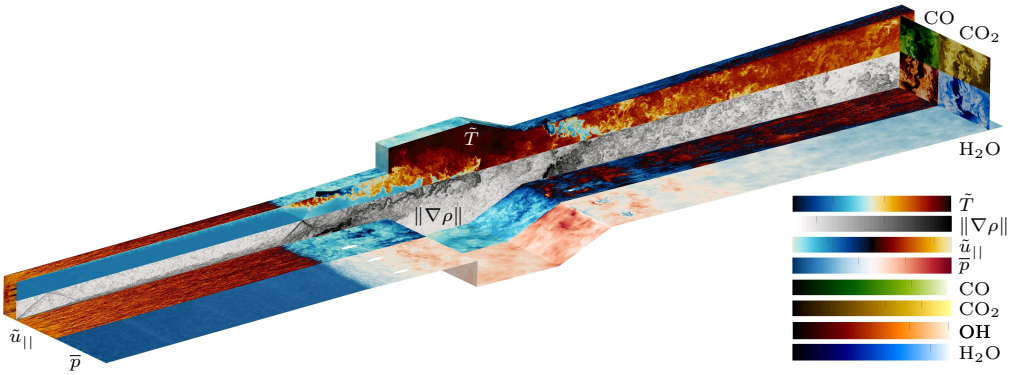

FIGURE 4. Three-dimensional view of instantaneous flow features from a snapshot of the fine-mesh simulation of the dual-mode ($M_f = 6.5$) operating regime. Temperature and magnitude of density gradient are shown on a vertical slice at $z = 38.1$ mm, containing a set of the primary and secondary injectors. The engine walls show the instantaneous wall pressure and the magnitude of the velocity field at the matching location between the wall-model and the LES grid. Near the exit of the combustor, a cross section shows contours of the concentration of CO, CO_2, H_2O and OH. Color bars, from top to bottom, represent: temperature (216–3300 K), magnitude of density gradient (5–1000 kg/m^4, log scale), magnitude of the wall-parallel velocity at the wall-model exchange location (0–1600 m/s), wall-pressure (60–350 KPa), CO concentration (0–0.27), CO_2 concentration (0–0.12), OH concentration (0–0.01), and H_2O concentration (0–0.09). Horizontal and vertical symmetries have been used.

The instantaneous pressure contours shown in Figure 5(f) reflect the establishment of a shock train inside the combustor. Looking at different, uncorrelated time instants of the medium-mesh simulation plotted in Figure 6, it is observed that the streamwise location of the shock train oscillates following the unsteadiness of the recirculation region upstream of the primary injector: as more fuel and fresh air are entrained in the recirculation region, combustion is enhanced therein (as seen by the temperature contours in Figure 6) and the pressure rise propagates upstream, translating the overall shock system. Note that the primary injection occurs subsonically for this operating regime.

Using tunable diode laser absorption spectroscopy (TDLAS), Brown *et al.* (2012) inferred temperature and water concentration fields at the combustor exit in the ground tests. Maximum temperature values of approximately 2800 K were found experimentally, occurring in the core of the engine; these agree with the values found in our simulations in that region. However, the adiabatic condition imposed in the simulations results in an increased temperature near the wall (approximately 3100 K). Besides the viscous heating in the boundary layers, the linear expansion of the ratio of specific heats assumed in the combustion model (see Section 3.1) might be responsible for an overprediction of temperature wherever the temperature of the flow differs significantly from the reference temperature provided by the flamelet library (which does not exceed 2800 K, as seen in Figure 2). This issue is currently being investigated. Additional simulations with isothermal walls are also under way.

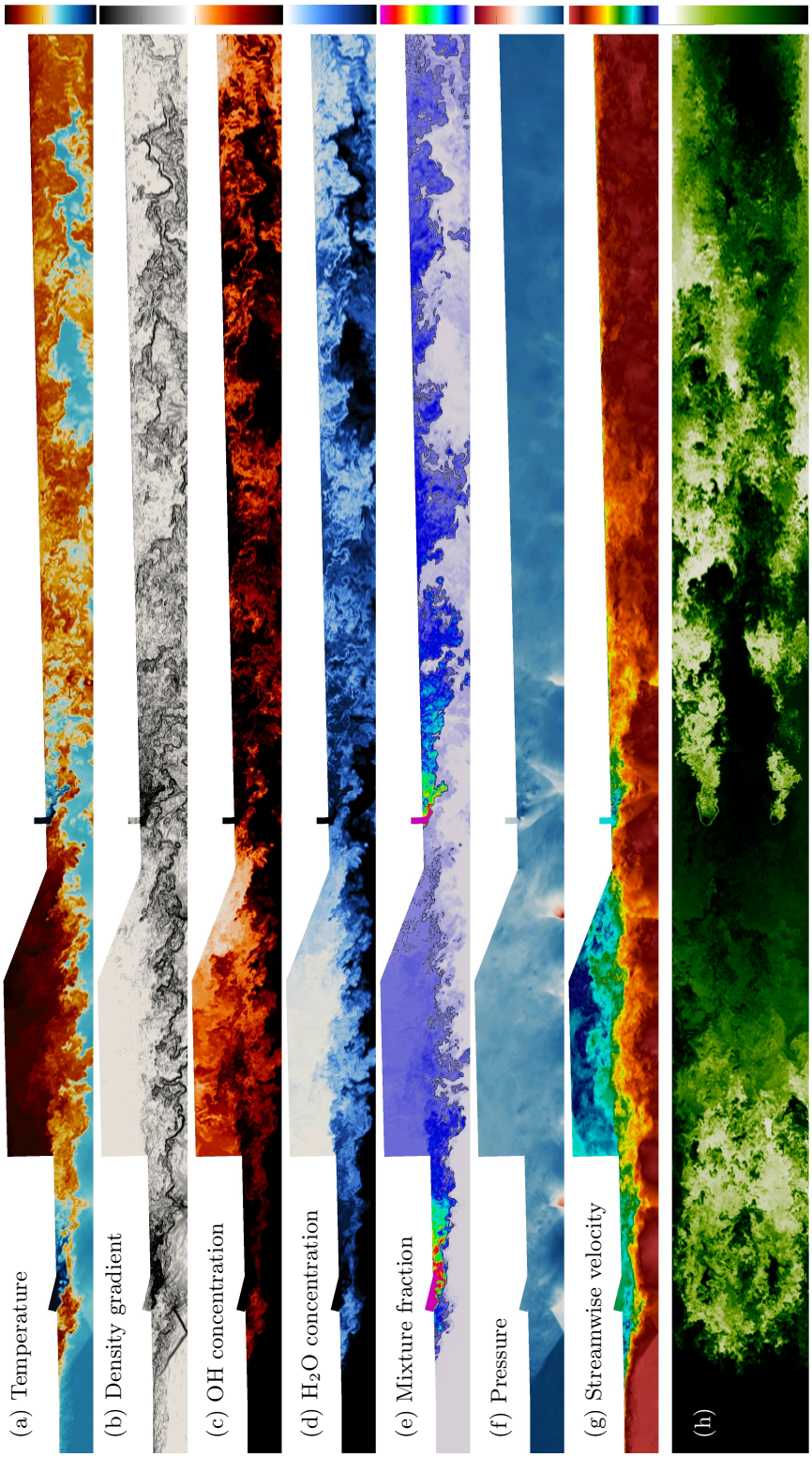

FIGURE 5. From top to bottom: contours of instantaneous temperature (215–3280 K), density gradient (15–500 kg/m^4, logscale), OH concentration (0–0.01), H_2O concentration (0–0.09), mixture fraction (0–1), pressure (77–773 KPa), streamwise velocity (-600–1615 m/s), and CO concentration (0–0.3) for the reacting-flow simulation in the dual-mode operating regime at $M_f = 6.5$. The bottom plot (h) contains a slice of the computational domain parallel to the wall of the combustor at a distance 2 mm normal to the wall. All other plots (a-g) are vertical slices at $z = 12.7$ mm passing through a set of injectors. For clarity most of the isolator has been left out of the visualization.

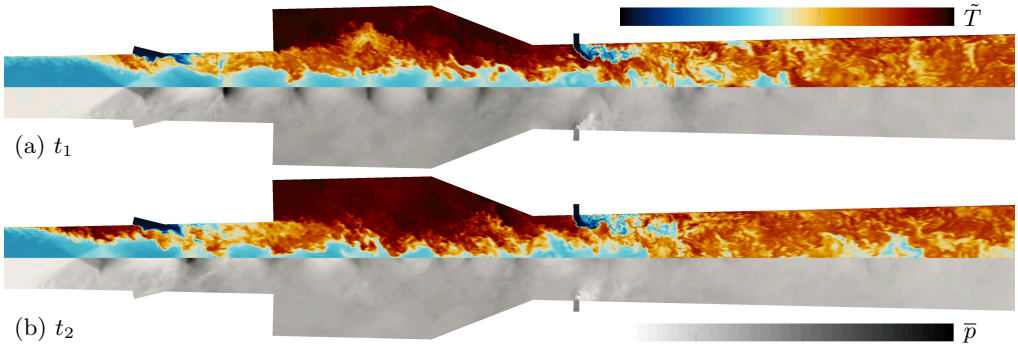

FIGURE 6. Contours of instantaneous temperature (215–3280 K) and pressure (77–774 KPa) on the vertical plane at $z = 12.7$ mm at two independent time steps of the simulation in the dual-mode regime at $M_f = 6.5$, showing the unsteadiness of the burning region upstream of the primary injector and the overall shock train inside the engine. Symmetry with respect to the horizontal ($y = 0$) plane has been used.

The effect of the sidewalls (only one is simulated, using symmetry) is shown in Figure 7 through instantaneous streamwise velocity contours on transverse planes at different streamwise locations inside the scramjet. The turbulent boundary layers on the top and sidewall flow near the exit of the isolator are discerned in Figure 7(a). We note that the same boundary layer thickness was assumed for both walls at the entrance of the isolator. At the primary injection stage (Figure 7b), the recirculation region on the top wall results in thicker boundary layers than on the side wall. Inside the cavity, strong three-dimensionality resulting from the sidewall can be observed in Figure 7(c), which significantly confines the region of highest streamwise velocity to the core of the cross section. At the secondary fuel injection stage (Figure 7d), the flow around the injector closer to the sidewall is largely disturbed by the surrounding lower-velocity region. This effect remains noticeable even half-way along the secondary combustor (Figure 7e), but is mitigated as the flow is accelerated towards the exit of the combustor (Figure 7f).

4.2.2. *Comparison between dual and scram modes*

Figure 8 shows a comparison between simulation results in the dual- and scram-mode operating regimes at $M_f = 6.5$ and 8.0, respectively. The instantaneous Mach number contours (Figure 8a) confirm that in the scram-mode, the flow remains fully supersonic along the core of the engine, with the subsonic flow regions mostly confined to the cavity and some patches in the wake of the jet downstream of the secondary injector. In the dual-mode, the shock-train inside the combustor extends upstream near the isolator, with subsonic flow dominating over a larger portion of the combustor and extending to the core of the engine. The recirculation region upstream of the primary injector for the dual-mode is not present in the scram-mode. The contours of CO concentration in Figure 8(b) suggest that the combustion of the fuel injected in the primary stage occurs rather differently between the two modes: in the dual-mode, the highest CO concentration levels occur shortly downstream of the primary injector (as it was also shown in Figure 6), decreasing inside the cavity; however, in the scram-mode simulation, only a thin layer of CO is visible immediately downstream of the primary injector, with most of the CO concentrating inside the cavity flameholder. Downstream of the secondary injector, the CO concentration levels and patterns appear similar between the two modes.

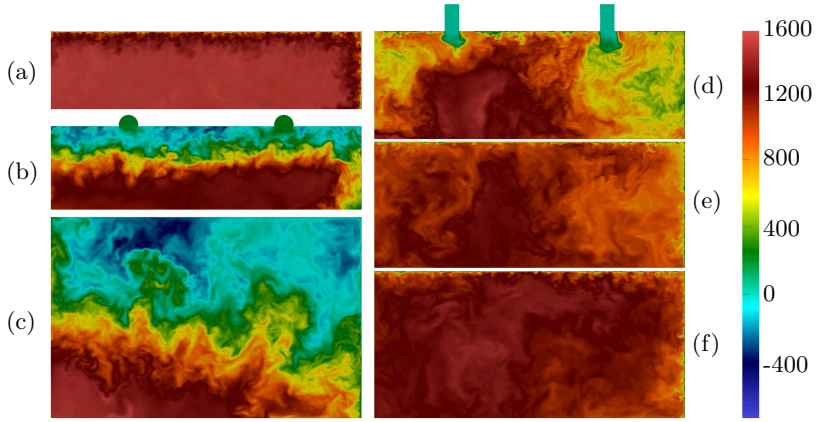

FIGURE 7. Contours of instantaneous streamwise velocity (m/s) for the simulation of the dual–mode regime at $M_f = 6.5$, on planes normal to the streamwise direction at locations: (a) near the exit of the isolator, $x = 190$ mm; (b) at the primary injection stage, $x = 243$ mm; (c) inside the cavity, $x = 333$ mm; (d) at the secondary injection stage, $x = 419$ mm; (e) near half-way inside the secondary combustor, $x = 550$ mm; (f) near the combustor exit, $x = 700$ mm. The bottom and left sides of each plot are the horizontal and vertical symmetry planes, respectively, whereas the top and right sides are the walls.

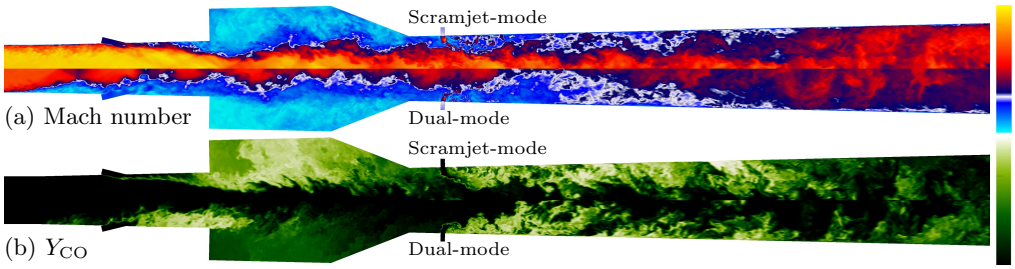

FIGURE 8. Contours of instantaneous Mach number (a) and CO concentration (b) on the spanwise-normal plane located at $z = 12.7$ mm. Each plot includes the results from the scram-mode ($M_f = 8$) and dual-mode ($M_f = 6.5$) simulations plotted on the half top and bottom parts, respectively, using the engine symmetry, for comparison. Colorbar for the Mach number from 0 to 3.6 (with the sonic line in white). Colorbar for Y_{CO} from 0 to 0.3.

5. Conclusions and future work

In this brief, we have presented our current efforts towards the numerical prediction of the flow inside the HIFiRE-2 scramjet engine by means of large-eddy simulations that incorporate wall and combustion models. Dual- and scram-mode operating regimes targeted in the flight test are simulated, for flight Mach numbers of 6.5 and 8, respectively. Comparisons with limited available experimental data from ground tests were presented.

Initial attempts to use a compressible FPVA combustion model were unsuccessful to provide enough burning throughout the combustor, which occurred only inside the cavity flameholder and at levels insufficient to provide the pressure rise observed experimentally. A simplified combustion model that assumes infinitely fast chemistry while still accounting for the subgrid fluctuations of the mixture fraction was then tested, resulting in much better agreement with the experimental data for the dual-mode regime. This suggests that the FPVA formulation originally used might not be able to fully account for the auto-ignition phenomenon for the chemical mechanism, flow conditions, and mesh reso-

lutions considered in this study. Simulations run on three meshes of increasing resolution appear to indicate that the results are not yet fully grid-converged.

The transition from dual- to scram-mode is being studied in the present simulations by imposing a sudden change of the inflow and injection conditions in order to reduce the otherwise unfeasible computational cost associated with the much longer transition time of the flight test. The drop of pressure levels between the two modes occurs over a short time span (<2 ms). Further time-averaging in the statistically stationary regime is required to assess the predictive capability of the current combustion model in the scram-mode.

Instantaneous flow features were explored, showing, for the $M_f = 6.5$ case, the presence of a recirculation region upstream of the primary injector that anchors a flame and produces the combustion-induced pressure rise in that region, as observed experimentally, and derives into a shock-train inside the combustor. Unsteadiness of this recirculation region translates into an oscillatory behavior of the shock train which moves upstream and downstream as dictated by the mixing and combustion of entrained incoming fresh air and injected primary fuel. Transverse planes showed that the flow inside the combustor is highly three-dimensional, particularly inside and downstream of the cavity flameholder. Comparison between the dual and scramjet simulations suggested a rather different location where the combustion of the fuel injected in the primary stage takes place.

Future work includes the assessment of flamelet-based models with additional dimensions (e.g., pressure and enthalpy). The sensitivity to the chemical mechanism and the characteristics of the incoming turbulent boundary layers will be evaluated. Simulations with isothermal walls and the full domain (i.e., without symmetries) will be pursued.

Acknowledgments

This work was supported by the Department of Energy under the Predictive Science Academic Alliance Program (PSAAP, grant DE-FC52-08NA28614). The authors are grateful to Parviz Moin, director of PSAAP at Stanford University, David Davidson (HTGDL at Stanford University), for providing the chemical mechanism used in this work, to Mark Gruber (AFRL), for references to the HIFiRE-2 HDCR ground tests and RANS simulations, and to Frank Ham for providing a version of the *CharLES* code on which the *CharLES*^{x} solver used in this work was originally based. The authors acknowledge computing time on the Mira and Tukey clusters at Argonne Leadership Computing Facility (ALCF), on the Sequoia and Vulcan clusters at Lawrence Livermore National Laboratory and on the Certainty cluster at Stanford (MRI-R2 NSF Award 0960306).

REFERENCES

Balaras, E., Benocci, C. & Piomelli, U. 1996 Two-layer approximate boundary conditions for large-eddy simulations. *AIAA J.* **34** (6), 111–1119.

Berglund, M. & Fureby, C. 2007 LES of supersonic combustion in a scramjet engine model. *Proc. Combust. Inst.* **31**, 2497–2504.

Bermejo-Moreno, I., Larsson, J., Campo, L., Bodart, J., Vicquelin, R., Helmer, D. & Eaton, J. 2011 Wall-modeled large eddy simulation of shock/turbulent boundary-layer interaction in a duct. In *Annual Research Briefs*, pp. 49–62. Center for Turbulence Research.

Brown, M. S., Herring, G. C., Cabell, K., Hass, N., Barhorst, T. F. & Gru-

ber, M. 2012 Optical Measurements at the Combustor Exit of the HIFiRE 2 Ground Test Engine. AIAA Paper 2012-0857.

Bynum, M. D. & Baurle, R. A. 2011 A Design of Experiments Study for the HIFiRE Flight 2 Ground Test Computational Fluid Dynamics Results. AIAA Paper 2011-2203.

Cabell, K., Hass, N., Storch, A. & Gruber, M. 2011 HIFiRE Direct-Connect Rig (HDCR) Phase I Scramjet Test Results from the NASA Langley Arc-Heated Scramjet Test Facility. AIAA Paper 2011-2248.

Cabot, W. 1995 Large-eddy simulations with wall models. In *Annual Research Briefs*, pp. 41–50. Center for Turbulence Research.

CEFRC 2013 Combustion Energy Frontier Research Center (CEFRC) Mechanism Version 0.9. `http://www.princeton.edu/cefrc/`.

Choi, H. & Moin, P. 2012 Grid-point requirements for large eddy simulation: Chapman's estimates revisited. *Phys. Fluids* **24** (011702).

Crow, A. J. 2013 Computational uncertainty quantication of thermal radiation in supersonic combustion chambers. PhD thesis, The University of Michigan.

Crow, A. J., Boyd, I. D. & Terrapon, V. E. 2012 Radiation modeling of a hydrogen fueled scramjet. *J. Thermophys. Heat Transfer* **1**, 11–21.

Cuda, V. & Hass, N. 2009 Heat Flux and Wall Temperature Estimates for the NASA Langley HIFiRE Direct Connect Rig. In *JANNAF 43rd Combustion; 31st Airbreathing Joint Meeting*, pp. 1–24. La Jolla, CA.

Donde, P., Koo, H. & Raman, V. 2012 A multivariate quadrature based moment method for LES based modeling of supersonic combustion. *J. Comput. Phys.* **231**, 5805–5821.

Doran, E. M. 2011 A multi-dimensional flamelet model for ignition in multi-feed combustion systems. PhD thesis, Stanford University.

Fulton, J. A., Edwards, J. R. & Hassan, H. A. 2012 Large-Eddy/Reynolds-Averaged Navier-Stokes Simulations of a Dual-Mode Scramjet Combustor. AIAA Paper 2012-0115.

Fureby, C. 2012 LES for supersonic combustion. AIAA Paper 2012-5979.

Hass, N., Cabell, K. & Storch, A. 2009 HIFiRE Direct Connect Rig (HDCR) Phase I Ground Tests Results from the NASA Langley Arc-Heated Scramjet Test Facility. In *JANNAF 43rd Combustion; 31st Airbreathing Joint Meeting*, pp. 1–24. La Jolla, CA.

Jackson, K. R., Gruber, M. R. & Buccellato, S. 2011 HIFiRE flight 2 overview and status update 2011. In *17th AIAA International Space Planes and Hypersonic Systems and Technologies Conference*, pp. 1–17. AIAA.

Kawai, S. & Larsson, J. 2012 Wall-modeling in large eddy simulation: length scales, grid resolution and accuracy. *Phys. Fluids* **24**, 15105.

Kawai, S. & Larsson, J. 2013 Dynamic non-equilibrium wall-modeling for large eddy simulation at high Reynolds numbers. *Phys. Fluids* **25**, 015105.

Khalighi, Y., Nichols, J. W., Lele, S., Ham, F. & Moin, P. 2011 Unstructured large eddy simulation for prediction of noise issued from turbulent jets in various configurations. In *17th AIAA/CEAS Aeroacoustics Conference*.

Klein, M., Sadiki, A. & Janicka, J. 2003 A digital filter based generation of inflow data for spatially developing direct numerical or large eddy simulations. *J. Comput. Phys.* **186**, 652–665.

Koo, H. 2011 Large-Eddy Simulations of scramjet engines. PhD thesis, The University of Texas at Austin.

Koo, H., Donde, P. & Raman, V. 2013 LES-based Eulerian PDF approach for the simulation of scramjet combustors. *Proc. Combust. Inst.* **34**, 2093–2100.

Larsson, J., Bermejo-Moreno, I., Bodart, J. & Vicquelin, R. 2012 Predicting the operability limit of the HyShot II scramjet using LES. In *Annual Research Briefs*, pp. 241–251. Center for Turbulence Research.

Larsson, J., Vicquelin, R. & Bermejo-Moreno, I. 2011 Large eddy simulations of the HyShot II scramjet. In *Annual Research Briefs*, pp. 63–74. Center for Turbulence Research.

Pellett, G. L., Dawson, L. C., Vaden, S. N. & Wilson, L. G. 2009 Nitric Oxide and Oxygen- Air Contamination Effects on Extinction Limits of Non-premixed Hydrocarbon-Air Flames for a HIFiRE Scramjet. In *JANNAF 43rd Combustion; 31st Airbreathing Joint Meeting*, pp. 1–24. La Jolla, CA.

Pečnik, R., Terrapon, V. E., Ham, F., Iaccarino, G. & Pitsch, H. 2012 Reynolds-Averaged Navier-Stokes Simulations of the HyShot II Scramjet. *AIAA J.* **8**, 1717–1732.

Pierce, C. D. 2001 Progress-variable approach for large-eddy simulation of turbulent combustion. PhD thesis, Stanford University.

Pierce, C. D. & Moin, P. 2004 Progress-variable approach for large-eddy simulation of non-premixed turbulent combustion. *J. Fluid Mech.* **504**, 73–97.

Pitsch, H. 2006 FlameMaster, A C++ Computer Program for 0D Combustion and 1D Laminar Flame Calculations. `http://www.stanford.edu/~hpitsch`.

Pitsch, H., Chen, M. & Peters, N. 1998 Unsteady flamelet modeling of turbulent hydrogen/air diffusion flames. *Proc. Combust. Inst.* **27**, 1057–1064.

Spalart, P. R. 2009 Detached-eddy simulation. *Annu. Rev. Fluid Mech.* **41**, 181–202.

Storch, A. M., Bynum, M., Liu, J. & Gruber, M. 2011 Combustor operability and performance verification for HIFiRE Flight 2. AIAA Paper 2011-2249.

Terrapon, V. E., Ham, F., Pečnik, R. & Pitsch, H. 2009 A flamelet-based model for supersonic combustions. In *Annual Research Briefs*, pp. 47–58. Center for Turbulence Research.

Terrapon, V. E., Pečnik, R., Ham, F. & Pitsch, H. 2010 Full-system RANS of the HyShot II scramjet Part 2: Reactive cases. In *Annual Research Briefs*, pp. 69–80. Center for Turbulence Research.

Touber, E. & Sandham, N. 2009 Large-eddy simulation of low-frequency unsteadiness in a turbulent shock-induced separation bubble. *Theor. Comput. Fluid Dyn.* **23**, 79–107.

Vreman, A. W. 2004 An eddy-viscosity subgrid-scale model for turbulent shear flow: Algebraic theory and applications. *Phys. Fluids* **16** (10), 3670–3681.

Wang, H., You, X., Joshi, A. V., Davis, S. G., Laskin, A., Egolfopoulos, F. & Law, C. K. 2007 USC Mech Version II. High-Temperature Combustion Reaction Model of H2/CO/C1-C4 Compounds. `http://ignis.usc.edu/USC_Mech_II.htm`.

Wang, M. & Moin, P. 2002 Dynamic wall modeling for large-eddy simulation of complex turbulent flows. *Phys. Fluids* **14** (7), 2043–2051.

Xie, Z.-T. & Castro, I. P. 2008 Efficient generation of inflow conditions for large eddy simulation of street-scale flows. *Flow Turbul. Combust.* **81** (3), 449–470.